Numerical modeling of the global semidiurnal tide in the present day and in the last glacial maximum

Gary D. Egbert
College of Oceanic and Atmospheric Sciences, Oregon State University, Corvallis, Oregon, USA

Richard D. Ray and Bruce G. Bills[1]
NASA Goddard Space Flight Center, Greenbelt, Maryland, USA

Received 20 May 2003; revised 14 November 2003; accepted 21 November 2003; published 2 March 2004.

[1] A hydrodynamic model incorporating a self-consistent treatment of ocean self-attraction and loading (SAL), and a physically based parameterization of internal tide (IT) drag, is used to assess how accurately barotropic tides can be modeled without benefit of data, and to explore tidal energetics in the last glacial maximum (LGM). M_2 solutions computed at high resolution with present day bathymetry agree with estimates of elevations from satellite altimetry within 5 cm RMS in the open ocean. This accuracy, and agreement with atlimetric estimates of energy dissipation, are achieved only when SAL and IT drag are included in the model. Solutions are sensitive to perturbations to bathymetry, and inaccuracies in available global databases probably account for much of the remaining error in modeled elevations. The $\approx$100 m drop in sea level during the LGM results in significant changes in modeled M_2 tides, with some amplitudes in the North Atlantic increasing by factors of 2 or more. Dissipation is also significantly changed by the drop in sea level. If IT drag estimated for the modern ocean is assumed, dissipation increases by about 50% globally, and almost triples in the deep ocean. However, IT drag depends on ocean stratification, which is poorly known for the LGM. Tests with modified IT drag suggest that the tendency to a global increase in dissipation is a robust result, but details are sensitive to stratification. Significant uncertainties about paleotides thus remain even in this comparatively simple case where bathymetry is well constrained. *INDEX TERMS:* 1255 Geodesy and Gravity: Tides—ocean (4560); 4560 Oceanography: Physical: Surface waves and tides (1255); 4267 Oceanography: General: Paleoceanography; 4568 Oceanography: Physical: Turbulence, diffusion, and mixing processes; *KEYWORDS:* tides, energy dissipation, Last Glacial Maximum

Citation: Egbert, G. D., R. D. Ray, and B. G. Bills (2004), Numerical modeling of the global semidiurnal tide in the present day and in the last glacial maximum, *J. Geophys. Res.*, *109*, C03003, doi:10.1029/2003JC001973.

1. Introduction

[2] The evolution of the moon's orbit is closely linked to the history of tidal dissipation in the ocean [e.g., *Hansen*, 1982; *Bills and Ray*, 1999]. This connection, and the clear evidence that tidal dissipation must have varied significantly over time, have spurred a number of efforts to model the ocean tides in the recent and distant past [e.g., *Thomas and Sündermann*, 1999, and references therein]. It is far from clear how reliable these model-based estimates of paleotides are, particularly given that bathymetry and the locations of shorelines are only crudely known in the increasingly distant past. Moreover, some models appear incapable of reproducing present-day tides with any degree of fidelity, a fact that should not be surprising if we consider that the basic mechanisms of tidal energy dissipation are still being debated [*Munk*, 1997]. Indeed, our considerable knowledge of present-day tides relies at least as much on the near-global measurements made possible by altimetry as on numerical modeling or theory. Before considering what the tides, and tidal dissipation, may have been in the past it is appropriate to ask how accurately we can model the tides of the present-day without benefit of direct tidal observations or data assimilation.

[3] Early efforts to model the present-day tides using very coarse grids and only partly known bathymetry [e.g., *Bogdanov and Mugarik*, 1967; *Pekeris and Accad*, 1969], led to global solutions which differed significantly amongst themselves, and which were only qualitatively consistent with what was then known about tides in the open ocean [*Hendershott*, 1977]. With the availability of TOPEX/Poseidon (T/P) altimeter data, tidal elevations in the deep ocean are now known with an accuracy of a few centimeters [*Shum et al.*, 1997; *Le Provost*, 2001], and it is now

[1] Also at Scripps Institution of Oceanography, La Jolla, California, USA.

0148-0227/04/2003JC001973$09.00

possible to assess quantitatively the accuracy of numerical tidal solutions.

[4] A great advance was the global finite-element solution of *Le Provost et al.* [1994]. The relatively close agreement of their solution with T/P measurements suggested that highly accurate solutions could be obtained with a purely hydrodynamic model, provided accurate bathymetry and numerical grids with sufficiently high resolution were used. However, Le Provost et al. solved their model equations separately for individual ocean basins, and then spliced together those results. Open boundary conditions for each basin were adjusted to achieve agreement with tide gauges, either informally or with a strong constraint data assimilation approach [*Lyard and Genco*, 1994]. Thus although their numerical solution satisfied the astronomically forced linearized shallow water equations (SWE) within each basin, the solution was not really independent of all data. Subsequent improvements to the finite element hydrodynamic code allowed simultaneous modeling of the full globe with no adjustable open boundary conditions. Initial applications of this code, with the traditional quadratic bottom friction drag parameterization, resulted in global solutions that fit the T/P data and validation tide gauges much more poorly (F. Lyard and C. Le Provost, personal communication, 1999), demonstrating the critical role played by data in the original 1994 solution. Indeed, all of the best present global tidal solutions are tightly constrained to fit T/P altimeter data.

[5] The altimeter data have also revealed a major shortcoming in the usual formulation of the SWE used for modeling barotropic tides. *Egbert and Ray* [2000, 2001] have shown that there is significant dissipation of tidal energy over rough topography in the open ocean, almost certainly due to conversion from barotropic to baroclinic waves. Since the inferred internal tide conversion amounts to roughly one third of the total tidal energy dissipation, accurate modeling of the barotropic tide will require accounting for this process, either by parameterizing the dissipation in the two-dimensional SWE [*Jayne and St. Laurent*, 2001; *Carrére and Lyard*, 2003], or with a full three-dimensional model of the stratified ocean. Experiments with the latter approach have been initiated (e.g., H. Simmons, personal communication, 2003), but owing to the small spatial scales associated with internal tides, the first approach is computationally more practical at this time.

[6] In this paper we describe our efforts to develop and test a global barotropic model which reproduces the present-day tidal elevation fields using only knowledge of bathymetry and the astronomical forcing, with no additional forcing or boundary condition constraints obtained from data. We use a straightforward modeling approach, based on finite difference time stepping of the nonlinear SWE, with a rigorous treatment of ocean self-attraction and loading (SAL), and several parameterizations of internal tide (IT) drag. Computations are done for a wide range of nearly global grids, with resolutions ranging from 1° to 1/12°. We also do experiments with small perturbations to our standard bathymetry, to test sensitivity of solutions to this critical input parameter. For all of the results reported here we focus on the principal lunar semidiurnal constituent M_2, although other constituents were included in the model runs to better represent nonlinear bottom drag in shallow water. Including a parameterization for IT drag significantly improves the fidelity of the solution. The best model results (5 cm RMS misfit between deep-ocean T/P elevations and the numerical model) are obtained with the highest resolution grid, and with rigorous treatment of ocean self-attraction and loading. The level of accuracy achieved is reasonably consistent with the effect of likely errors in the currently best available bathymetry.

[7] After validating our solution for the modern oceans, we consider the effect of dropping the sea level to that estimated for the last glacial maximum (LGM). The IT drag parameterization we use depends on ocean stratification, and it is not clear how this should be changed for the LGM. We test several scenarios, including stratification similar to the modern ocean, and significant reductions and increases in stratification. As we shall show, the effects of LGM sea level changes are much larger than errors in the modern solutions, with total tidal dissipation increasing in our LGM model solutions by up to 50%. However, details of these solutions depend on assumptions about ocean stratification.

2. Hydrodynamic Modeling

2.1. Finite-Difference SWE

[8] We assume shallow water dynamics [e.g., *Hendershott*, 1977]

$$\frac{\partial \mathbf{U}}{\partial t} + \mathbf{f} \times \mathbf{U} + \mathbf{U} \cdot \nabla \mathbf{u} + a_H \nabla^2 \mathbf{U} + gH\nabla(\zeta - \zeta_{\mathrm{SAL}}) + \mathcal{F} = \mathbf{f}_0 \quad (1)$$

$$\frac{\partial \zeta}{\partial t} = -\nabla \cdot \mathbf{U}, \quad (2)$$

where ζ is the tidal elevation; $\mathbf{U}$ is the volume transport vector, equal to velocity times water depth H; $\mathbf{f}$ is the Coriolis vector (oriented to the local vertical), $\mathcal{F}$ is the frictional or dissipative stress, and the term $a_H\nabla^2\mathbf{U}$ is a crude parameterization of horizontal turbulent eddy viscosity.

[9] In initial tests we experimented with a range of values of a_H centered around 10^3 m^2 s^{-1}. Elevations in the open ocean were found to be insensitive to the exact value of a_H unless it was increased by several orders of magnitude. Although *Thomas and Sündermann* [1999] [see also *Zahel*, 1980] found empirically that $a_H = 10^5$ m^2 s^{-1} produced the most realistic solutions in their global tidal modeling studies, the large lateral momentum transfer implied by such large viscosities is difficult to justify physically [e.g., *Colbo*, 2002] and much smaller values of this parameter are typically assumed [e.g., *Wunsch et al.*, 1997]. For modeling tides, this horizontal viscosity can be justified primarily for numerical stability, and should probably be kept as small as grid resolution allows. The large values of a_H used in some previous tidal modeling studies probably improved solutions by increasing dissipation in deep ocean areas, compensating for inadequacies in the parameterization of other dissipative processes.

[10] M_2 solutions in the deep ocean were in fact changed only slightly if the nonlinear advective terms in equation (1) are omitted. With advection omitted we found that a_H could be reduced to zero with little effect. Thus for most of the high resolution numerical experiments described below the advective and turbulent viscosity terms were omitted to reduce run times. The astronomical tide generating force, which includes perturbations caused by the Earth's body

tide [*Hendershott*, 1972] is denoted by $\mathbf{f}_0$. We included up to 8 constituents (M_2, S_2, N_2, K_2, K_1, O_1, P_1, Q_1) in $\mathbf{f}_0$. However, very similar results were obtained for M_2 when the forcing was restricted to the dominant semidiurnal and diurnal constituents M_2 and K_1, so only these two constituents were included for most of the extensive modeling experiments described here.

[11] Tidal loading and self-attraction [*Hendershott*, 1972; *Ray*, 1998] are accounted for by the term ζ_{SAL}, which we consider in more detail below. We solve the system of equations (1) and (2) numerically on a C-grid, following the finite difference time stepping approach described in *Egbert et al.* [1994]. All grids are nearly global, covering the area from 86°S to 82.25°N. Bathymetry was interpolated (and smoothed where appropriate) from a combination of the 1/30° *Smith and Sandwell* [1997] database in deep water and equatorward of 72°, ETOPO5 [*National Geophysical Data Center*, 1992] in shallow areas and the Arctic, and a new compilation of bathymetry for the Antarctic (L. Padman, personal communication, 2001). Boundary conditions at the coast were zero normal flow. Open boundary conditions at the small northern boundary of the domain in the Arctic were specified elevations, taken from the global FES94 solution [*Le Provost et al.*, 1994]. Tests with variants, including the Arctic assimilation solutions of *Kivman* [1997], and a rigid wall at the top of the domain, showed that elevations outside the Arctic were nearly independent of the details in these boundary conditions. Recent modifications to our modeling code allow more general spherical coordinate systems with both poles over land, and make time stepping of the SWE over the full globe possible. Limited tests of this approach on the full globe with no open boundaries also resulted in little change from the nearly global solutions.

[12] The dissipation term $\mathcal{F} = \mathcal{F}_B + \mathcal{F}_{IT}$ included components for bottom boundary layer drag in shallow seas and IT wave radiation. The first component was parameterized in the usual way as quadratic in velocity

$$\mathcal{F}_B = (c_D \parallel \mathbf{v} \parallel /H)\mathbf{U}, \tag{3}$$

where $\mathbf{v}$ is the total velocity vector (in our model, all tidal constituents), and the value of the nondimensional parameter c_D is approximately 0.0025. Tests with c_D in the range 0.001–0.01 showed that deep-water elevations were only weakly sensitive to the exact value of this parameter.

2.2. Parameterization of Internal Tide Drag

[13] *Bell* [1975] derived an expression for energy conversion from barotropic to baroclinic tides by small amplitude sinusoidal topography of amplitude h and wave number κ

$$E_f = \frac{(\omega^2 - f^2)^{1/2}}{2\omega}\rho_0\kappa h^2 N u^2, \tag{4}$$

where N is the buoyancy frequency, ρ_0 the mean ocean density, f the Coriolis parameter, ω the tidal frequency, and u the barotropic tidal velocity perpendicular to the topography. *Jayne and St. Laurent* [2001] used equation (4) to develop a simple IT drag parameterization for global tidal modeling. They estimated the height of the scattering topography as the RMS of bathymetric variations not resolved by their 1/2° numerical grid, and, ignoring the dependence on tidal frequency ω, obtained a spatially varying linear drag coefficient

$$c_{IT} = \frac{1}{2H}\kappa h^2 N. \tag{5}$$

The buoyancy frequency N (the value at the ocean bottom is most appropriate for nonuniform stratification [see *Llewelyn-Smith and Young*, 2001]) was obtained from *Levitus* [1999], and the wave number κ was left as a tunable parameter. Note that c_{IT} is just the linear drag coefficient required to match the energy loss to the barotropic tide given by equation (4). *Jayne and St. Laurent* [2001] found that including this extra drag term in their implementation of the SWE (with $\kappa \approx 2\pi/10\mathrm{km}$) significantly improved the fit of modeled tidal elevations to those estimated from T/P. *Carrére and Lyard* [2003] report similar improvements in tidal solution accuracy when a qualitatively similar parameterization of IT drag was incorporated into their global finite element model.

[14] We tested the scheme of *Jayne and St. Laurent* [2001], along with two variants. The first of these is based on the work of *Sjöberg and Stigebrandt* [1992], who give an alternative (but dimensionally similar) expression for barotropic energy conversion. In this approach the conversion (comparable to E_f of equation (4)) is calculated by treating the bottom topography as a series of discrete steps and applying theories developed for generation of internal waves by flow over sills. Note that in this approach energy conversion is calculated for each step independently, and that this can only be formally justified if the steps are far enough apart. Expressions for energy flux away from each topographic step are given in *Sjöberg and Stigebrandt* [1992] and are summarized in *Gustafson* [2001]. The resulting expressions for E_f again depend quadratically on the cross-step tidal velocity, so a linear drag coefficient c_{IT} is readily derived as for the Bell formula (4). This second approach has no obvious unknown or tunable parameters, but in fact the expression for E_f can be shown to depend strongly on the grid resolution used to define the steps [*Garrett et al.*, 2002]. For our calculations we used a 1/12° grid to define the topographic steps, and stratification profiles from *Levitus* [1999] to compute the IT drag. In numerical experiments with this parameterization it was found necessary to allow for an extra tunable scaling factor to obtain the best results, although the optimal scaling factor was of order one.

[15] The third approach we tried is based on an extension of the theory of Bell to allow for two-dimensional topography and a finite-depth ocean [*Llewellyn Smith and Young*, 2001]. As with *Bell* [1975] the theory is based on linear inviscid dynamics, and small amplitude topography is assumed on an otherwise (locally) flat bottom. In the Appendix we show that in the small amplitude limit the internal tide radiation stress at a fixed tidal frequency is linearly related to the barotropic volume transports via convolution in space with a 2×2 tensor

$$\mathcal{F}_{IT} = \mathcal{R}_\omega * \mathbf{U}/H, \tag{6}$$

where the kernel $\mathcal{R}_\omega$ is readily calculated given the stratification and bathymetry, using the results presented in *Llewellyn Smith and Young* [2001]. Although linear in the transports, the relation is nonlocal in space, and since the

dissipation operator $\mathcal{R}_\omega$ is frequency dependent, also in time. As it would be extremely expensive to fully implement this convolution in a numerical scheme for solving the time dependent SWE, we implemented this scheme only approximately, replacing the convolution of equation (6) with local multiplication by a 2×2 drag tensor. For this last approach there are no tunable parameters. Further details are given in the Appendix.

[16] The second and third approaches, which are rather similar to that used by *Carrére and Lyard* [2003], appear to be qualitatively different from the classical Bell formula used by *Jayne and St. Laurent* [2001] in that they parameterize IT drag in terms of resolved topographic gradients instead of unresolved bottom roughness. However for all three IT drag parameterizations the energy flux scales quadratically with topographic amplitude and tidal velocity, and linearly with bottom stratification and topographic wave number, as in equation (4). Thus in practice the spatial patterns of IT drag coefficient variations are very similar in all cases, with the IT drag largest in the open ocean over rough topography, in most of the same areas where *Egbert and Ray* [2000, 2001] empirically mapped significant deep-water dissipation in the barotropic tide. Provided scaling parameters (e.g., κ in equation (5)) were chosen to optimize fit of the tidal solution to T/P constrained elevations, we found that all three IT drag parameterizations performed similarly. For results described in the remainder of the paper we use the third approach, outlined in the Appendix. In addition to producing reasonable results without any tunable parameters, this variant has the potential advantage of providing an anisotropic tensor representation of the IT drag. This refinement should allow a more realistic treatment of IT drag in some areas, such as along the continental shelf edge where IT drag coefficients should be large for cross-shelf but not along-shelf flows.

2.3. Implementation of the SAL Correction

[17] The importance of ocean tide self-attraction and loading (SAL) in global hydrodynamic models has been realized since the mid-1970s [*Hendershott*, 1972; *Gordeev et al.*, 1977]. In equation (1) the effects of SAL are included as an extra equilibrium-like tide ζ_{SAL}, which can be related to ζ through convolution with the SAL Green's function [e.g., *Hendershott*, 1972; *Ray*, 1998]

$$\zeta_{\mathrm{SAL}} = \mathcal{G}_{\mathrm{SAL}} * \zeta. \tag{7}$$

Substituting equation (7) into equation (1) results in an integro-differential equation. Applying the full convolution operator of equation (7) at each time step is not computationally practical, so other nonexplicit solution strategies are required. For the modern ocean a bootstrap approach is possible: given a reasonable approximation to ζ, ζ_{SAL} can be computed once and added to equation (1) as an extra forcing term. This approach, with elevations from *Schwiderski* [1978], was used by *Le Provost et al.* [1994]. The same approach, using more accurate T/P constrained elevations to estimate ζ_{SAL}, has been used for global data assimilation solutions by *Le Provost et al.* [1998] and *Egbert and Erofeeva* [2002]. However, solutions computed in this way are not really independent of all data, and the computed elevation fields will not in general be consistent with the assumed ζ_{SAL}. This inconsistency can lead to significant imbalances in the energy equation [e.g., *Le Provost and Lyard*, 1997]. More seriously, this simple approach cannot be applied to calculations with different ocean geometries, where tidal elevations may deviate significantly from the modern estimates of ζ available to compute ζ_{SAL}.

[18] Another simple approach that has frequently been used is to approximate convolution with $\mathcal{G}_{\mathrm{SAL}}$ with multiplication by a scalar factor β. In this case $\zeta - \zeta_{\mathrm{SAL}}$ is replaced by $(1 - \beta)\,\zeta$ and equation (1) is again reduced to a partial differential equation. Analysis by *Accad and Pekeris* [1978] suggested $\beta \approx 0.085$; *Schwiderski* [1978] used $\beta = 0.1$. However, as pointed out by *Ray* [1998] this approximation is crude, and in any event no fixed scalar β is appropriate for all locations in the ocean. To allow a more rigorous data-free treatment of SAL in global modeling *Hendershott* [1972] suggested an iterative solution approach, with elevations ζ^n from iteration n used in equation (7) to compute ζ^n_{SAL}, and then the result used in equation (1) as an additional forcing to compute ζ^{n+1}. Unfortunately, numerical experiments suggested that convergence of this scheme could not be guaranteed [*Hendershott*, 1972, 1977]. We tested this iterative approach for the modern ocean, starting from an initial guess at ζ^0_{SAL}estimated from an accurate T/P based model (TPXO.5). The RMS change in elevations $|\zeta^n - \zeta^{n-1}|$ between successive iterates is plotted as a dashed line in Figure 1a. Differences increase with each iteration, so the scheme is not converging.

[19] A slightly modified iterative approach, which was first suggested by *Accad and Pekeris* [1978], converges rapidly. The idea is to write

$$\zeta_{\mathrm{SAL}} = \beta\zeta + (\mathcal{G}_{\mathrm{SAL}} * \zeta - \beta\zeta) = \beta\zeta + \mathcal{G}'_{\mathrm{SAL}} * \zeta, \tag{8}$$

where β is chosen to be a reasonable scalar SAL approximation. At iteration $n + 1$ we then replace $\zeta - \zeta_{\mathrm{SAL}}$ in equation (1) with $(1 - \beta)\,\zeta^{n+1} - \mathcal{G}'_{\mathrm{SAL}} * \zeta^n$. It is readily verified that if this converges as $n \to \infty$, ζ^n converges to the solution of the full integro-differential equation. The change between successive iterates for this modified scheme (using $\beta = 0.1$) shows convergence in 4–5 iterations (solid line in Figure 1a). Note that ζ_{SAL} computed from TPXO.5 was used to initialize both schemes, so the first iteration is the same in both cases. For some of the results discussed below, where sea levels are dropped to LGM levels, ζ deviates significantly from the modern T/P constrained elevations. In this case, our initial choice of ζ_{SAL} is a poor approximation, and additional iterations are required for convergence.

[20] In Figure 1b we plot the total work done by the SAL term in the tidal equations

$$W_{\mathrm{SAL}} = \left\langle \rho g \int \zeta_{\mathrm{SAL}}\, \partial\zeta/\partial t \, dS \right\rangle. \tag{9}$$

Since we assume an elastic Earth (with Love numbers strictly real) $\mathcal{G}_{\mathrm{SAL}}$ is also real and the cycle average, denoted by the brackets $\langle\rangle$ of the global integral must be zero [e.g., *Hendershott*, 1972]. W_{SAL} (computed with ζ obtained from iteration n and ζ_{SAL} from iteration $n - 1$) is plotted in Figure 1b. For the first iteration W_{SAL} is nearly 0.5 TW, a significant fraction of the 2.5 TW of M_2 tidal dissipation.

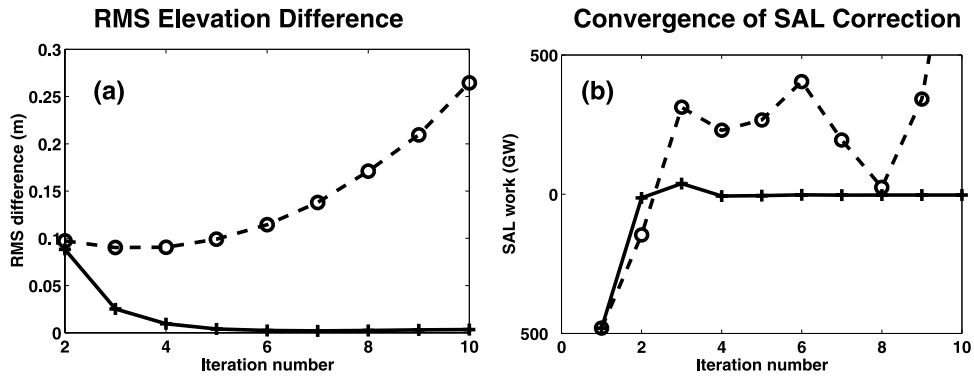

Figure 1. Convergence of iterative schemes for ocean self-attraction and tidal loading. (a) Global RMS difference in elevation between successive iterates. Dashed line indicates iterative scheme proposed by *Hendershott* [1972]. Solid line indicates modified scheme (following equation (8)) of *Accad and Pekeris* [1978]. (b) Convergence of global integral of SAL work term (9) for the simple (dashed lines) and modified (solid lines) iterative schemes.

For the modified (but not the simple) iterative scheme W_{SAL} converges rapidly to zero, further demonstrating the consistency of ζ_{SAL} and ζ obtained in this way.

3. Results

[21] Using the numerical hydrodynamic model described above we ran a series of tidal simulations for the modern ocean, varying grid resolution and model parameters, including bathymetry. To assess accuracy of the solutions we compare model elevations to TPXO.5, an updated version of the global tidal inverse solution described in *Egbert et al.* [1994]. We emphasize comparison to areas where the reference elevations are most accurate, in the deep open ocean, and equatorward of 66° where T/P data are available.

3.1. Effect of Grid Resolution

[22] The RMS difference between M_2 elevations computed with the hydrodynamic model and the T/P reference solution are plotted as a function of grid resolution in Figure 2. Increasing resolution of the finite difference grid significantly improves agreement between model outputs and elevations inferred from T/P. This is true for model runs with and without an IT drag parameterization, and in deep and shallow water (Figure 2a). Including IT drag significantly reduces misfits for all resolutions. The best results, with misfits in deep water ($H > 1000$ m) slightly below 5 cm RMS, are obtained with IT drag run at 1/12° resolution. Including shallow seas in the comparison increases misfits somewhat (thinner lines in Figure 2a). Only slightly worse results are obtained with a grid resolution of 1/8°. To reduce computation times we used this resolution for most of the numerical experiments discussed below.

[23] For the results presented in Figure 2 IT drag was parameterized in terms of the linear drag tensor **R** defined in the Appendix, without adjusting any parameters. Very similar results were obtained with the other two IT drag parameterizations discussed above, but in these cases some tuning of the overall scale of the IT drag was required. For the scheme based on *Bell*'s [1975] formula (i.e., 5) results were best for a value of $\kappa \approx 10^{-3}\mathrm{m}^{-1}$, slightly larger than the optimal value $\kappa \approx 2\pi \times 10^{-4}\mathrm{m}^{-1}$ found by *Jayne and St. Laurent* [2001]. For the second scheme IT drag coef-

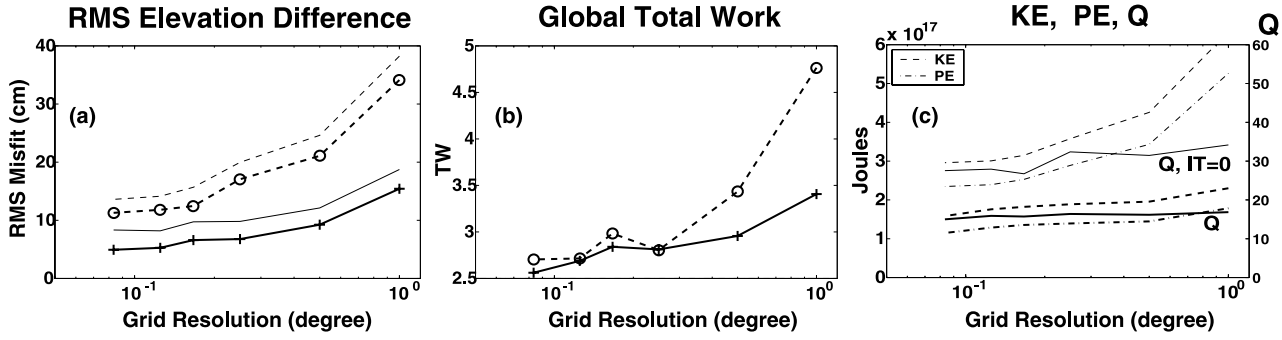

Figure 2. (a) RMS difference between M_2 elevations from the global inverse solution TPXO.5, and hydrodynamic solutions computed for a range of grid resolutions, equatorward of 66°. Solid and dashed lines are for computations with and without internal tide drag, respectively. Heavy lines give misfits for deep ($H > 1000$ m) water; light lines for all depths. (b) Global integral of work done by the M_2 tidal potential, for solutions with (solid lines) and without (dashed lines) internal tide drag. (c) Global integral of kinetic and potential energy, and Q as a function of model grid resolution. In panel (c) heavy lines are for models run with internal tide drag, light lines are for models with no internal tide drag.

Table 1. Potential, Kinetic Energy, and Q for M_2[a]

	TPXO.5	GOT99	0 ka IT	0 ka no IT	20 ka IT	20 ka IT × .5	20 ka IT × .25	20 ka IT × 2
PE ($\times 10^{17}$ J)	1.28	1.29	1.23	2.32	3.76	5.21	6.87	2.48
KE ($\times 10^{17}$ J)	1.78	1.89	1.76	3.01	4.65	6.24	8.02	3.19
Q	17.7	18.2	15.6	27.6	29.3	38.4	50.7	21.6

[a]TPXO.5 and GOT99 are constrained by T/P data, the other six are purely numerical solutions discussed in the text.

ficients derived from *Sjöberg and Stigebrandt* [1992] (computed using bathymetry on a 1/12° grid and stratification from *Levitus* [1999]) worked best when multiplied by a factor of 0.75. Note also that our results obtained with and without IT drag are comparable to those reported by *Carrére and Lyard* [2003] in similar experiments with incorporating IT drag into a high resolution global finite element model.

[24] Although our focus here is on the dominant semidiurnal M_2 constituent, we also always obtained solutions for the dominant diurnal constituent K_1. At the highest resolution the RMS misfit to the T/P constrained elevations was 1.9 cm in the deep ocean when IT drag was used, and 2.3 cm when it was omitted. Thus even though the IT drag coefficients, which should in principle depend on frequency, are most appropriate for semidiurnal constituents, we also achieve some improvement in accuracy for diurnal constituents.

3.2. Energetics of the Hydrodynamic Solutions

[25] The work done by the tidal potential, which for an energetically consistent model must equal the global tidal energy dissipation, can be computed as [e.g., *Hendershott*, 1972]

$$W = \left\langle \rho g \int \zeta_{EQ}\, \partial\zeta/\partial t \, dS \right\rangle \tag{10}$$

(we again neglect the small Earth-tide dissipation). W approaches the well constrained modern value of approximately 2.45 TW [*Egbert and Ray*, 2001] as the numerical grid is refined (Figure 2b). For lower grid resolutions the agreement is significantly better when the IT drag parameterization is used. For the better resolved grids similar values of the global dissipation total are obtained with and without IT drag.

[26] However, there are significant differences in the model energetics at all resolutions. When IT drag is omitted from the model, potential and kinetic energies are roughly a factor of two higher (Table 1), and these global integrals are much more sensitive to grid resolution (Figure 2c). Vertically integrated M_2 kinetic energy is plotted in Figure 3. Tidal currents in the Pacific are in particular significantly more energetic if the IT drag term is omitted. Kinetic energy

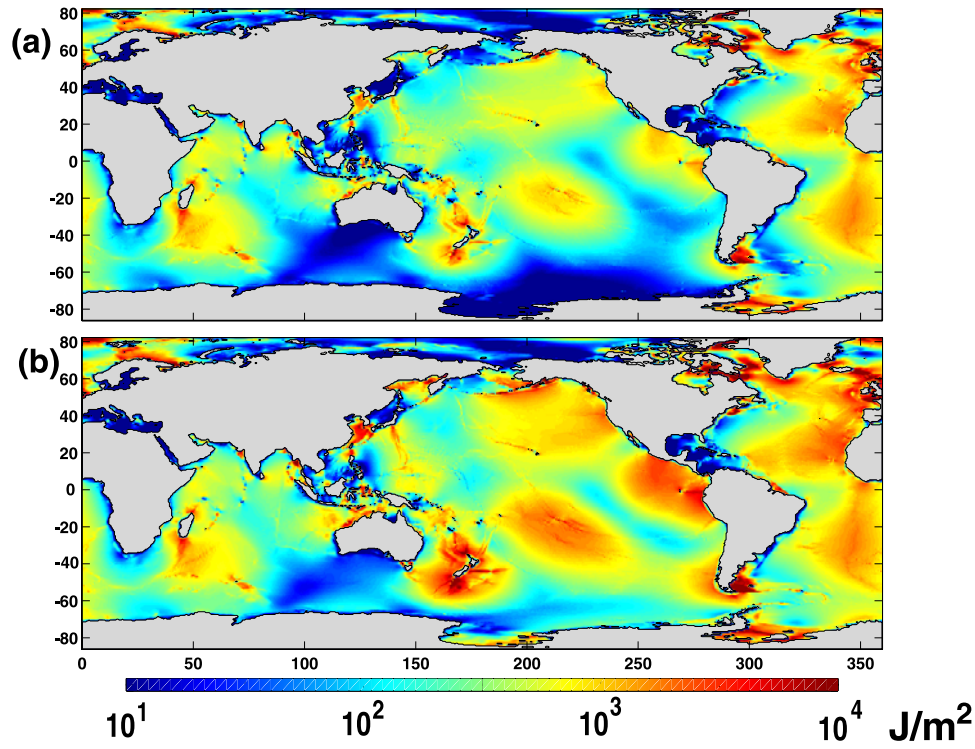

Figure 3. Map of vertically integrated M_2 kinetic energy for solutions computed (a) with and (b) without IT drag parameterization. Note that a logarithmic scale is used to display the wide range in tidal kinetic energies.

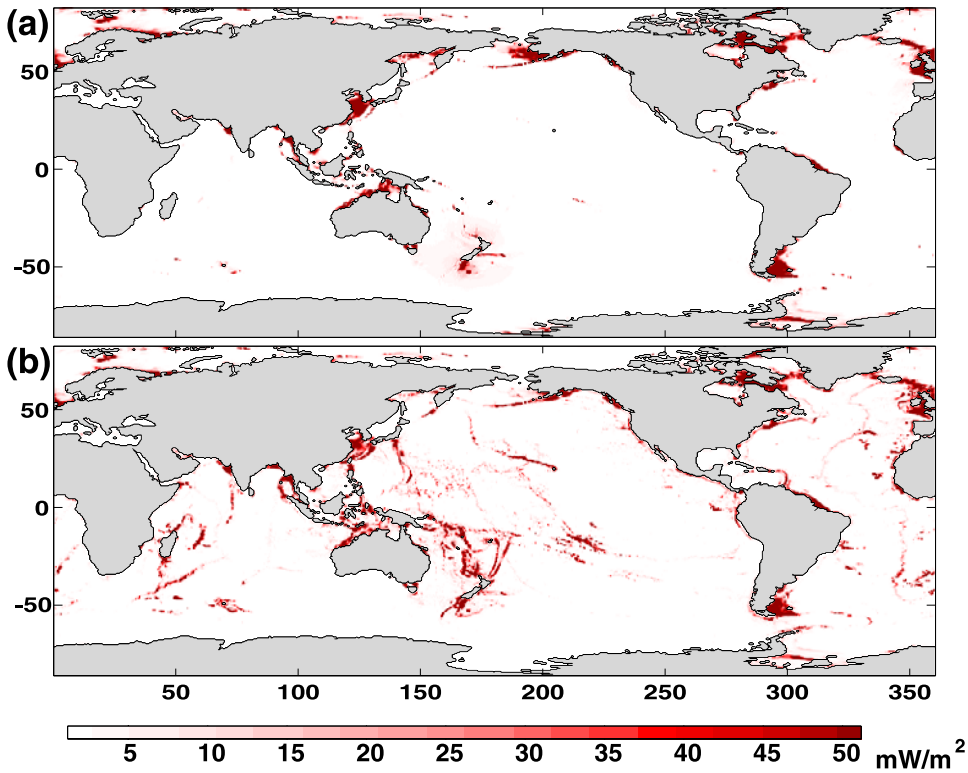

Figure 4. Map of M_2 dissipation computed as the balance between energy flux divergence and work terms for numerical solutions computed using present-day bathymetry (a) without and (b) with the IT drag parameterization.

increases less in the Atlantic, and there is little change in the Indian Ocean. The nondimensional dissipation timescale $Q = \omega(\mathrm{KE} + \mathrm{PE})/W$ also increases quite significantly, from 16 with IT drag to around 30 without (Table 1, Figure 2c). Estimates of Q obtained from models constrained by T/P data are all around 18–20 for semidiurnal tides.

[27] The spatial distribution of dissipation is of course also strongly affected by the inclusion of IT drag. Following the approach of *Egbert and Ray* [2001] we computed maps of dissipation for the numerical solutions as a local balance between energy flux divergence and work done by the tide generating force and SAL (Figure 4). As could be anticipated, when the IT drag parameterization is omitted (Figure 4a) nearly all dissipation occurs in a small number of marginal shallow seas. Inclusion of a parameterization for IT drag leads to substantial additional energy dissipation in the deep ocean over rough topography (Figure 4b).

[28] The pattern of enhanced dissipation in Figure 4b is qualitatively similar to the empirical maps presented by *Egbert and Ray* [2000, 2001], but with dissipation more localized and focused in the numerical solution plotted here. For a more quantitative comparison to dissipation inferred from T/P we consider integrals over individual shallow seas and selected patches of the deep ocean. These are presented in Figure 5 for the ocean areas defined in *Egbert and Ray* [2001, Figure 2] for the 1/8° numerical solutions with and without IT drag, and for three of the empirical T/P estimates discussed in *Egbert and Ray* [2001]. A rough breakdown between total shallow sea and deep ocean dissipation is given in Table 2. Including IT drag brings the spatial distribution of M_2 energy dissipation into much better agreement with the

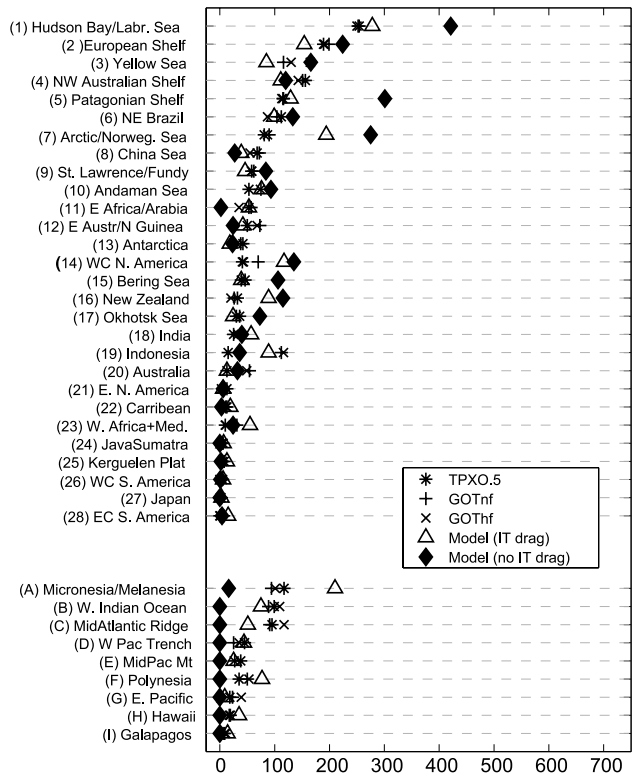

Figure 5. Energy dissipation integrated over shallow seas and selected deep ocean areas defined in *Egbert and Ray* [2001, Figure 2], for solutions computed with and without IT drag. For comparison three empirical T/P estimates of dissipation (TPXO.5, GOT99hf, GOT99nf) are plotted.

Table 2. Dissipation for M_2 (in TW) in Deep and Shallow Seas, Following the Division Given in *Egbert and Ray* [2001][a]

	TPXO.5	GOT99hf	GOT99nf	0 ka IT	0 ka no IT	20 ka IT	20 ka IT × .5	20 ka IT × .25	20 ka IT × 2
Shallow	1.63	1.72	1.88	2.10	2.65	2.45	2.59	3.54	1.88
Deep	.81	.73	.57	.58	.06	1.51	1.50	1.04	1.82
Total	2.44	2.45	2.45	2.68	2.71	3.96	4.19	4.59	3.70

[a]TPXO.5, GOT99hf and GOT99nf are constrained by T/P data, the other six are purely numerical solutions discussed in the text.

empirical estimates. Most obviously, including the IT drag parameterization increases dissipation in the deep ocean area of *Egbert and Ray* [2001] from a negligible level to about 25% of the total, in rough agreement with the T/P estimates (Table 2). The distribution among deep-sea areas is also for the most part in reasonable agreement with the T/P estimates (Figure 5). The addition of IT drag (primarily in the deep sea) also changes the pattern of dissipation in shallow seas, improving agreement with the empirical estimates (Figure 5). Without IT drag the numerical model dissipates significantly more energy in some major shallow sea sinks (e.g., Hudson Bay/Labrador Sea, Patagonian Shelf, Bering Sea) than is indicated by the T/P solutions. Dissipation in these shallow areas is reduced to more reasonable levels by allowing for IT drag in the deep ocean.

[29] Even with IT drag there remain discrepancies between dissipation in the hydrodynamic solution and the empirical estimates. Some of this disagreement can be attributed to uncertainties in the correct distribution of dissipation in the modern ocean, as suggested by the scatter in the three T/P estimates. Note in particular that areas around Indonesia are poorly constrained by the T/P data, as discussed in *Egbert and Ray* [2001]. However, there are some anomalous areas including the Arctic/Norwegian Sea, the Northwest Coast of North America, and around New Zealand, where differences between the numerical model dissipations and the tightly clustered T/P estimates are significant. In all of these areas the numerical models significantly exceed the T/P based dissipation estimates. In deep water, areas in the South Pacific (Micronesia/Melanesia and Polynesia) come out high in the numerical solution with IT drag, while the Mid-Atlantic and W. Indian Ridges come out low. This suggests that our simple linear IT parameterization overestimates drag produced over the larger scale topography associated with volcanic arcs and island chains, and underestimates drag over oceanic spreading centers, which are dominated by smaller spatial scales and are spread over a larger area. Overall there is less deep ocean dissipation in the numerical model than in the T/P estimates (Table 2). Much of the additional dissipation in the empirical estimates is spread over the deep ocean, not necessarily near major topographic features. This difference may reflect in part the poor spatial resolution of the empirical estimates, but it also perhaps indicates some inadequacy in our parameterization of deep ocean dissipation. For example, scattering into internal waves by seamounts or small-scale bottom roughness may be poorly accounted for in our parameterization, perhaps due to violation of the small-amplitude topography assumption, and/or inadequacies in currently available bathymetric data.

3.3. Sensitivity to Errors in Bathymetry

[30] Figure 2 suggests that further increases in model grid resolution will lead to little improvement in fit to the observed modern tidal elevations. A number of factors probably limit the accuracy that can be expected from numerical solution of the SWE at any resolution. For example, the IT drag parameterizations we have tested are all based on a linear treatment appropriate to small amplitude topography. Even for this simplified linear case a proper treatment of IT drag would involve convolution with a nonlocal operator (see the Appendix), so we have only incorporated IT drag approximately. The parameterization of bottom drag in terms of (3) with a constant c_D must also be only approximately correct. And of course, even for the modern ocean, there are potentially significant errors in the available bathymetric databases.

[31] To test the sensitivity of model solutions to uncertainties in the bathymetry we ran a series of simulations with small random perturbations to our standard bathymetry. To save computer time these runs were all done on a 1/4° grid. Several scenarios for the bathymetry errors were considered. For the first case the random variations were 5% of the local depth, with a decorrelation length scale of 2.5°. For the second case error amplitudes were increased to 10%, and for the third case variable error magnitudes were assumed, with a dependence on depth modeled on the statistics of differences between the *Smith and Sandwell* [1997] and ETOPO5 [*National Geophysical Data Center*, 1992] databases: $H < 100$ m: 25%; 100 m $< H <$ 200 m: 15%; 200 m $< H <$ 1000 m: 10%; 1000 m $< H <$ 3000 m: 6%; $H > 3000$ m: 3%. For cases 2 and 3 the decorrelation length scale of the bathymetric errors remained 2.5°. In each case 10 perturbed bathymetric grids were generated, solutions were calculated for each, and the global RMS elevation differences (relative to the standard 1/4° bathymetry solution) were computed. We also computed the RMS deviation in energy dissipation for each suite of perturbed bathymetry models. Results are summarized in Table 3.

[32] It is difficult to assess the accuracy of the available bathymetry. However, even if errors are only half the size of the difference between the Smith and Sandwell and ETOPO5 databases (an optimistic assessment, since the two databases are not independent at small and large scales), Table 3 suggests that in the open ocean errors in modeled M_2 tidal elevations exceeding 3 cm should be expected. Given the other shortcomings in the numerical SWE model, the 5 cm RMS error achieved by our 1/12° M_2 global

Table 3. Root Mean Square Changes in M_2 Tidal Elevations and in Total Energy Dissipation, for Random Variations of Bathymetry

Case	Global RMS, cm	Deep Ocean RMS, cm	Work RMS, TW
5% errors	3.23	2.69	0.037
10% errors	8.17	6.65	0.107
Variable errors	8.23	6.67	0.128

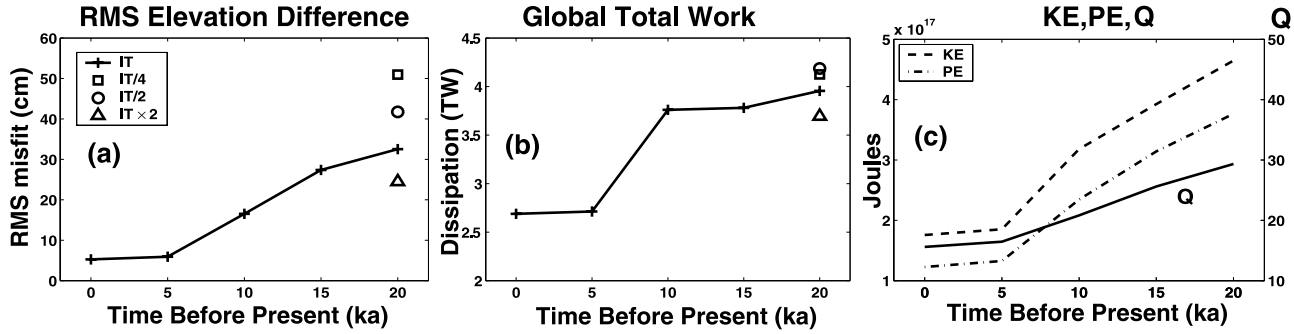

Figure 6. (a) RMS difference between M_2 tidal elevations determined from T/P and those computed with bathymetry adjusted using the ICE-4G model for selected epochs over the past 20 ka. (b) Work done by the tidal potential in these numerical solutions. (c) Potential and kinetic energies, and Q. The symbols at 20 ka in Figures 6a and 6b correspond to solutions computed with the linear IT drag coefficient multiplied by scalar factors indicated in the legend for Figure 6a.

solution is probably already close to the limit of accuracy that can be achieved at present.

[33] The high sensitivity of model outputs to bathymetry suggests that it will be difficult to model ocean tides accurately in the distant past, since bathymetry seems unlikely ever to be known well enough. On a more positive note, the total dissipation in the numerical models is not so sensitive to the small errors in bathymetry considered here. For all cases considered RMS variations in dissipation were less than 5% of the total. Thus for the recent past, where the gross geometry of the ocean basins is reasonably well known, model estimates of total dissipation should remain meaningful.

3.4. M_2 Tides in the Last Glacial Maximum (LGM)

[34] With the hydrodynamic model tuned to model the present-day ocean tides, we consider the effect of dropping sea level to that inferred for the LGM. For these experiments model bathymetry was modified using the 1° ICE-4G model [*Peltier*, 1993, 1994] which provides ocean depth and ice cover on a 1° grid for each millennium over the past 20 ka. For each epoch considered we first computed the difference in ocean depth with the present-day (0 ka) ICE-4G topography. The difference fields were then interpolated onto our 1/8° nearly global grid, and added to the present-day bathymetry. In this manner we made sea level adjustments consistent with the resolution of ICE-4G, but retained the higher resolution bathymetric details of the modern topography. In Figure 6a we plot the RMS difference between the present-day tidal elevations (as determined by T/P), and the elevations computed for a series of times over the past 20 ka. M_2 elevations for the present-day and 20 ka solutions are given in Figure 7. These results strongly suggest that M_2 tidal elevations in the LGM were indeed significantly different.

[35] Figure 6b shows M_2 tidal dissipation computed using equation (10) for numerical solutions every 5 ka over the past 20 ka. A large increase in dissipation, by almost 50%, accompanies the drop in sea level which exposed many of the shallow shelf areas where present-day dissipation is greatest. Kinetic and potential energies, also increased dramatically in the LGM numerical solutions (Figure 6c), and Q almost doubles from around 15 at 0 ka to nearly 30 at 20 ka.

[36] For most of our LGM computations we used IT drag coefficients estimated for the modern ocean. In fact, the IT drag depends linearly on the abyssal buoyancy frequency ($N = \sqrt{(g\rho_0 \partial_z \bar{\rho})}$) which could well have been significantly different during the LGM [e.g., *Adkins et al.*, 2002; *de Vernal et al.*, 2002]. The nature of these variations is at present poorly constrained, so we must content ourselves with tests of several rough hypothetical scenarios, with increased and reduced stratification. To do this we focus on the 20 ka bathymetry and simply multiply the IT drag coefficients based on the modern stratification by a spatially uniform scalar factor. For the first two cases we reduce the IT drag coefficients by factors of 2 and 4, corresponding to significant reductions in the buoyancy frequency N. This results in further significant changes in tidal elevations (Figure 6a), and an increase in global M_2 dissipation to over 4 TW (Figure 6b; Table 2). Q is also increased dramatically by a decrease in stratification, reaching a rather astounding value of 50 for the IT/4 case (Table 1). For the third case we increased the IT drag coefficient by a factor of 2, corresponding to an increase in ocean stratification. In this case total dissipation and Q are reduced (Tables 1 and 2), and elevations become more similar to those of the present-day (Figure 6).

[37] In Figure 8 we plot vertically integrated M_2 kinetic energy densities for the 20 ka model solutions with IT drag coefficients based on modern stratification, and reduced by a factor of 4. Kinetic energy densities for the 20 ka solutions are significantly larger in much of the ocean in both cases (compare to Figure 3). Increases are especially great in the North Atlantic. M_2 elevations in the 20 ka model solution exceed 3–4 m over much of the Labrador Sea, and off the Atlantic coasts of Spain and North Africa (Figure 7). Reducing the IT drag coefficient results in further increases in tidal amplitudes throughout much of the Atlantic. With IT drag based on modern stratification, tidal amplitudes increase only modestly in the Pacific when sea level is dropped. When IT drag is also reduced by a factor of 4 kinetic energies increase dramatically over much of the Pacific, especially off the northeast coast of Australia and around New Zealand. Thus tidal amplitudes in the Pacific are relatively more strongly controlled by deep ocean

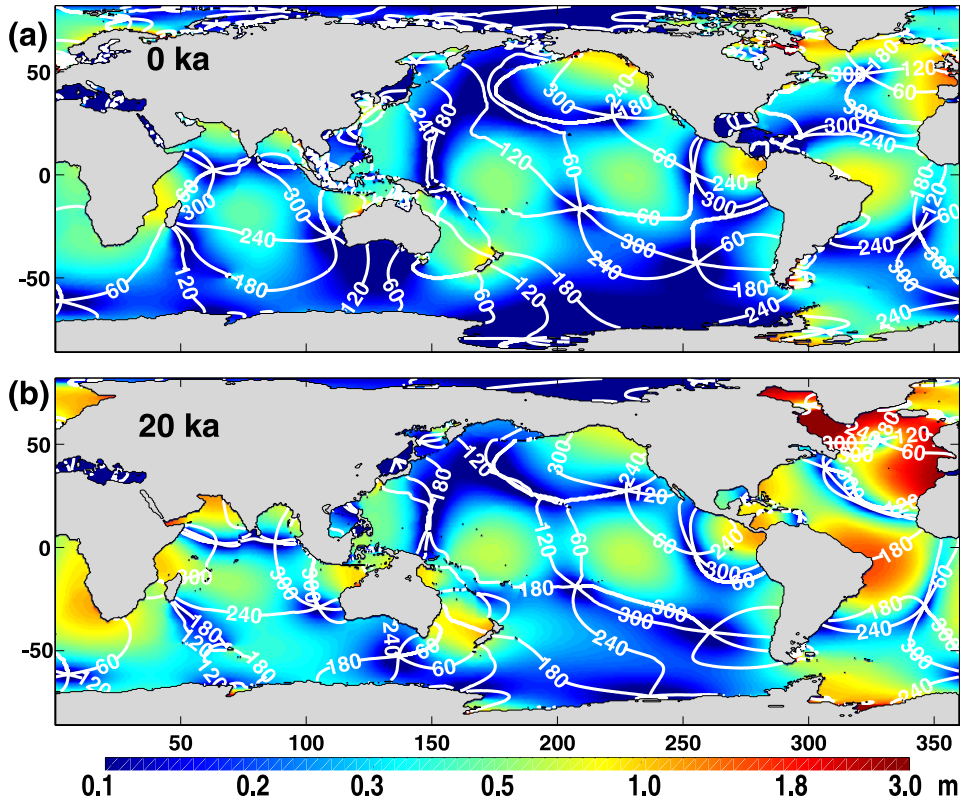

Figure 7. M_2 amplitude and phase for model solutions computed using bathymetry for (a) present-day and (b) 20 ka. For both solutions IT drag parameters estimated from modern day stratification are used. Note that the amplitude scale is nonlinear.

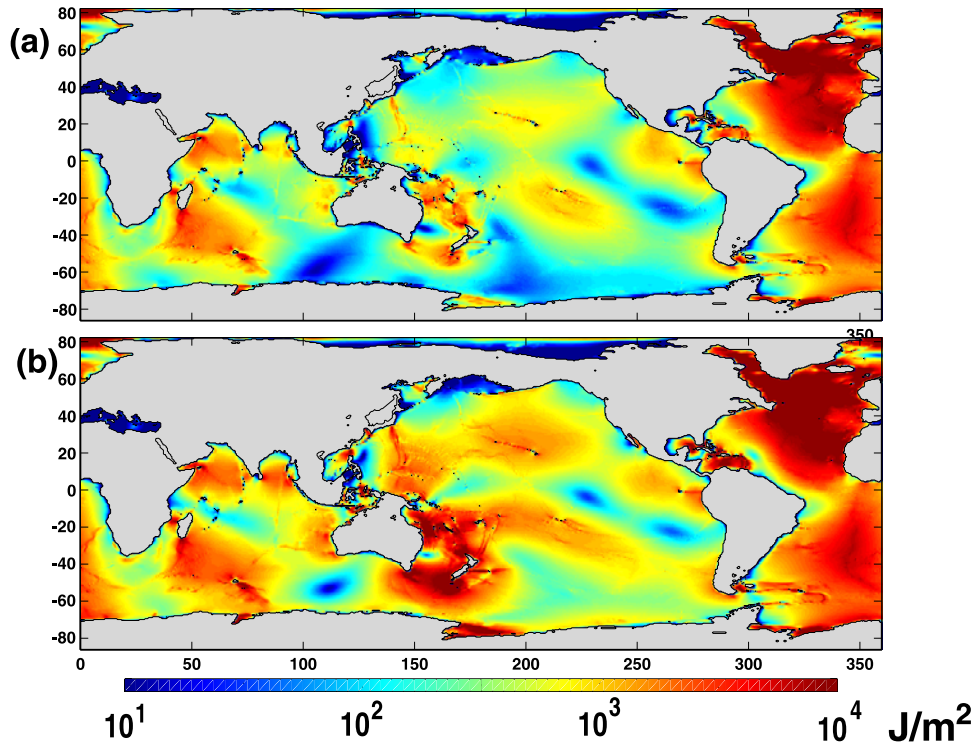

Figure 8. Map of vertically integrated M_2 kinetic energy for two 20 ka bathymetry solutions (a) with IT drag coefficients estimated from present-day stratification, and (b) with IT drag reduced by a factor of 4.

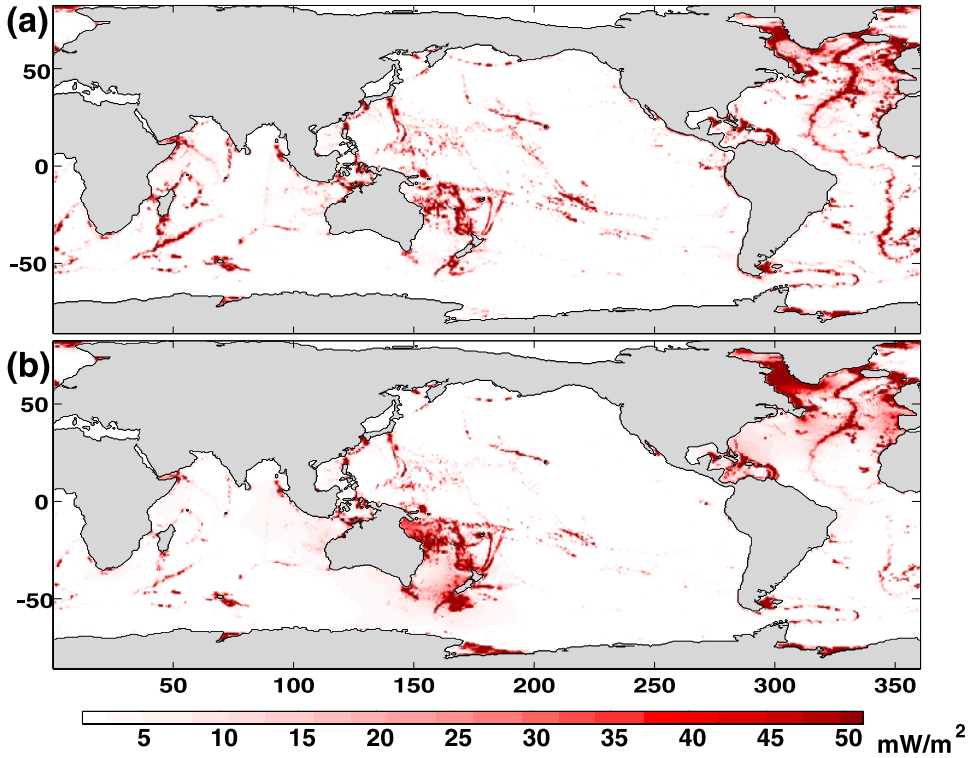

Figure 9. Dissipation maps computed for two of the 20 ka numerical solutions computed as the balance between energy flux divergence and work terms. (a) 20 ka bathymetry with IT drag coefficients estimated from present-day stratification, and (b) with IT drag reduced by a factor of 4.

dissipation (and hence stratification), while amplitudes in the Atlantic are more directly sensitive to sea level.

[38] The division of tidal energy dissipation between shallow and deep areas is given for the four 20 ka solutions in Table 2, and dissipation maps for two of the 20 ka cases are presented in Figure 9. Comparison to present-day solutions (Table 2; Figure 4) reveal that dramatic changes in the distribution of tidal dissipation result from the drop in sea level during the LGM. Some of the major shallow sea sinks in the present-day ocean are significantly reduced in area, and as a result would dissipate little energy. These include the Yellow Sea, the shelf off the northeast coast of Brazil, and the Patagonian Shelf. Dissipation is also significantly reduced over the European shelf and in the Gulf of Maine off the east coast of North America. However, at the same time deep ocean dissipation is significantly increased in the North Atlantic (especially over the mid-Atlantic ridge, off the northwest coast of Africa, and over the volcanic arc on the eastern edge of the Caribbean).

[39] Weakening stratification (which reduces the efficiency of internal wave conversion; see (4)) results in less deep-sea dissipation (Table 2). However, the reductions in IT drag coefficients are counterbalanced by increases in tidal currents (Figures 3 and 8), so that reducing IT drag by a factor of 4 result in deep ocean dissipation reduced by only a factor of 1.5 (Table 2). In fact, reducing stratification actually results in increases in deep ocean dissipation in some parts of the North Atlantic, and in the South Pacific around New Zealand and the Northeast coast of Australia (Figure 9). The increases in tidal currents associated with reductions in IT drag also result in increases in shallow sea dissipation, especially in the North Atlantic, and in the Ross and Weddell Seas, explaining the overall increase in total dissipation with decreasing N.

[40] Dissipation is broken down by ocean basin for five of the numerical solutions in Figure 10a. The fraction of dissipation occurring in the deep part of each basin is given in Figure 10b. Note that here the division between deep and shallow ocean is defined by the 1000 m isobath. This differs from the division used for Table 2, which follows the division used by *Egbert and Ray* [2001] to allow direct comparison with the empirical T/P estimates. For the empirical estimates shallow sea boundaries were drawn conservatively and well into the open ocean, to avoid complex topography where errors in the empirical tidal models were expected to be greatest. Deep ocean fractions in Figure 10b are thus somewhat greater than those of Table 2.

[41] For the present-day ocean basins the numerical model with IT drag dissipates about 750 GW in the North Atlantic, roughly consistent with the T/P estimates [*Egbert and Ray*, 2001]. Only a bit over 10% of this dissipation occurs in the deep ocean. When sea level is dropped to the 20 ka level (dashed lines) the fraction of dissipation in the deep ocean increases to roughly 40% for the weakest stratification (IT/4) case, and to nearly 60% for the case of increased stratification (IT $\times$ 2) case. Total dissipation in the North Atlantic is also increased dramatically by the drop in sea level. For the case where stratification is weakest the total dissipation in the model North Atlantic solution increases by a factor of 3, to more than 2.2 TW, almost equaling the M_2 dissipation in the entire present-day ocean.

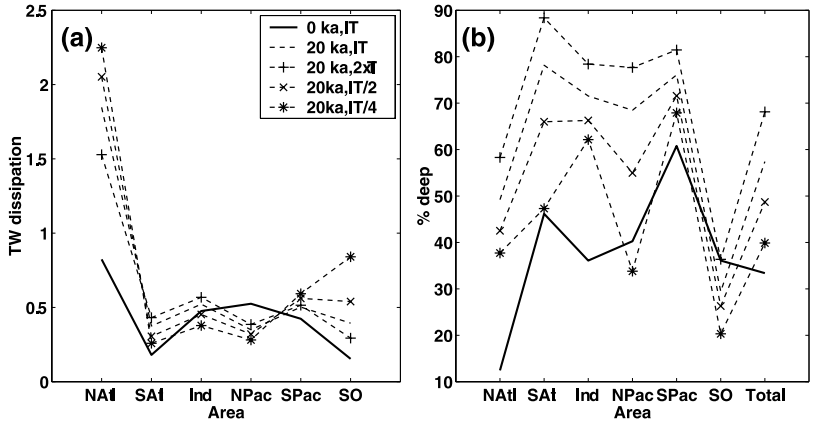

Figure 10. (a) Total energy dissipation in each ocean basin for five numerical solutions, including modern bathymetry and stratification, and 20 ka bathymetry with different stratification assumptions. (b) Fraction of dissipation in the deep ocean ($H > 1000$ m) for each basin, and the global total, for the five models of Figure 10a.

[42] Changes to dissipation in the other basins are generally more modest. In all scenarios considered dissipation is reduced in the North Pacific, and increased in the South Atlantic, South Pacific and Southern Ocean. The effect of stratification also varies between basins, with stronger stratification yielding higher dissipation in the South Atlantic, Indian, and North Pacific Basins. Not surprisingly, the percent of dissipation occurring in the deep ocean is always greatest when stratification is strongest. For the total over all basins almost 70% of the dissipation occurs in the deep ocean for LGM sea levels under the increased stratification scenario, and even with N reduced by a factor of 2 almost 50% of the dissipation is in the deep ocean. Only in the Southern Ocean is the fraction of dissipation in shallow seas increased under LGM conditions.

[43] Finally, we note that in our model runs the effect of lowering sea level in the LGM was significantly different for the diurnal constituent K_1. For K_1 there are still relatively significant changes in modeled tidal elevations due to the change in bathymetry. For example the RMS discrepancy between the modern day T/P constrained elevations and the model solution for this basin increases from 1.9 cm for the 0 ka run to 4 cm for the 20 ka run. However, dissipation varies by only about 5%, with a small decrease in the LGM. A complete exploration of this difference between semidiurnal and diurnal constituents is beyond the scope of this paper. However, a major contributing factor is undoubtedly the very different spatial distribution of dissipation for diurnal and semidiurnal species. For diurnal constituents, over half of the dissipation occurs in a small number of marginal seas around the North Pacific (the Okhotsk, China and Bering Seas [*Egbert and Ray*, 2003]). Aside from the Bering Sea, most of these sinks are still present during the LGM. In the North Atlantic, where the effects of dropping sea level are most dramatic for M_2, diurnal tides are very weak and dissipate little energy in the modern ocean.

4. Discussion

[44] Our results show that a purely hydrodynamic barotropic model of sufficiently high resolution can reproduce present-day tidal elevations with an RMS error of roughly 5 cm in the deep ocean. The global total M_2 tidal energy dissipation in the numerical solution, and the spatial distribution of this dissipation, are in reasonable agreement with empirical estimates inferred from T/P altimeter data. Both a rigorous self-consistent treatment of self-attraction/loading and some sort of parameterization of barotropic/baroclinic energy conversion are required to obtain solutions of this accuracy.

[45] The quality of the tidal solution depends critically on the accuracy of the bathymetry. Sensitivity tests with randomly perturbed bathymetry suggest that uncertainties in even the present-day bathymetry probably still limit our ability to model tidal elevations to about the level we have achieved here. This high sensitivity to details in the bathymetry places severe limits on the accuracy of tidal models for the distant past, in eras with poorly known bathymetry. Our approximate linear theory for computing IT drag is probably another major limitation on the accuracy of our numerical model. Improvements in the parameterization of IT drag may improve tidal models for the present-day ocean somewhat. However, our efforts to refine simple parameterizations which have been tried previously by *Jayne and St. Laurent* [2001] had little impact on the overall quality of the tidal solutions. The need for an accurate representation of internal wave drag presents further challenges to modeling of paleotides, since ocean stratification in even the recent past is poorly constrained.

[46] Our success with the present-day tides gives us some hope for modeling tides in the LGM, when at least the bathymetry is reasonably well constrained. Running our numerical model with bathymetry appropriate to the LGM results in significant changes in tidal fields with generally larger amplitudes, especially in the North Atlantic. The total global M_2 dissipation in the model increases by up to 50%, and the fraction of dissipation occurring in the deep ocean increases significantly. However, details in the magnitude and spatial pattern of these changes are sensitive to the assumed IT drag, which depends on the poorly known stratification. In general, reducing stratification increases total dissipation, but this effect varies between ocean basins. With reduced stratification and the LGM bathymetry, mod-

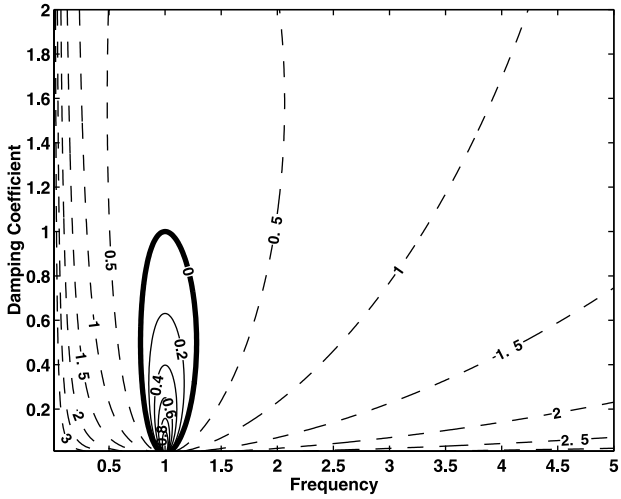

Figure 11. $\log_{10} W_H$ for the simple damped harmonic oscillator contoured as a function of (nondimensional) forcing frequency and damping coefficient (arbitrary units).

eled tidal dissipation in the North Atlantic increases to a rather astonishing 2.2 TW.

[47] It is worth bearing in mind that all of the dissipation in our model is an approximate parameterization of unresolved physics. These parameterizations are apparently sufficiently representative of actual loss of energy from resolved barotropic motions to allow quantitatively accurate modeling of the M_2 tide. However, it is not clear that our parameterization would be as appropriate to conditions of the LGM, particularly if tidal amplitudes were significantly increased. Perhaps under these circumstances other dissipative processes would become important. Thus while the general trends we have found are probably reliable, our quantitative estimates for tidal energetics in the LGM should not be taken too literally. Geological data that could confirm or contradict the very large tidal amplitudes predicted by our model for the LGM would be most welcome.

[48] It may be counterintuitive that changes to the model such as decreasing the area of shallow seas where most dissipation is localized, or reducing IT drag coefficients, actually lead to significant increases in total dissipation. This result can be understood with reference to the simple forced damped harmonic oscillator described by the equation

$$\partial_{tt} u + u + \gamma \partial_t u = \sin \omega t. \tag{11}$$

Here γ is a linear damping coefficient and ω the forcing frequency. The rate of energy dissipation for the harmonic oscillator of equation (11) is readily found to be

$$W_H = \frac{1}{2} \Re\left[i\omega / \left(1 - i\gamma\omega - \omega^2\right)\right] \tag{12}$$

W_H is contoured in Figure 11 as a function of ω and γ. Near resonance (ω = 1) dissipation increases as the damping coefficient decreases. Far from resonance the dependence on γ is reversed. As is well know [e.g., *Platzman et al.*, 1981] there are a number of normal modes of the tidal equations near the M_2 frequency. Several of these modes are predominantly localized in the North Atlantic, leading to resonant amplification of semidiurnal tides in this basin. Thus reducing the effective damping by exposing shallow sea energy sinks (or reducing stratification) might actually be expected to increase dissipation in this basin, as we find in our model study.

[49] Resonance effects can also explain the amplification of dissipation in the seas around New Zealand when stratification is reduced in the 20 ka model. As discussed in *Platzman et al.* [1981] the Kelvin wave around New Zealand is nearly resonant at the semidiurnal period. This wave dominates mode 38 (with a period of 10.8 hours) in the Platzman et al. compilation of global normal modes. The fact that dissipation in this area is increased significantly only in the cases where stratification is reduced suggests that this mode is primarily damped by dissipation in the deep ocean due to IT radiation drag.

[50] Our results may also have broader implications for the meridional overturning circulation (MOC). It is often assumed that the strength of the MOC is controlled by the downward convective arm of the circulation forced by vertical density contrasts at high latitudes. However, as summarized in *Wunsch* [2003], there are strong thermodynamic and fluid-dynamical arguments that the MOC must be mechanically driven, and hence controlled more directly by the strength of diapycnal mixing at lower latitudes. It is possible that the tides may provide half of the mechanical energy required for this mixing [*Munk and Wunsch*, 1998; *Egbert and Ray*, 2000], and thus variations in tidal amplitudes might be expected to impact the MOC. Based primarily on evidence from radiocarbon ages of North Atlantic Deep Water, it is widely believed that the overturning circulation in the North Atlantic was weaker in the LGM. As discussed by *Wunsch* [2003] this conclusion is somewhat surprising, since there is evidence that winds were stronger in the LGM. Stronger winds would be expected to strengthen the wind-forced ocean circulation, and they could possibly strengthen the wind-forced component of vertical turbulent mixing (although recent simulations by *Schmittner et al.* [2002] suggest otherwise). *Wunsch* [2003] speculated that, regardless of the wind influence, tidally induced mixing might have increased in the LGM, owing to an increase in deep-ocean tidal dissipation when shallow-sea energy sinks are removed by dropping sea levels. Our modeling results support Wunsch's suggestion. In all stratification scenarios we have considered, globally averaged barotropic tidal kinetic energies and deep ocean dissipation were significantly greater for LGM bathymetries.

[51] It is worth bearing in mind, however, that effects of dropping sea level vary significantly between ocean basins. Areas where tides are near resonance (e.g., the North Atlantic, around New Zealand for M_2) are much more sensitive to changes in sea level or stratification. Thus the spatial distribution of tidally driven mixing may have been very different in the LGM than it is in the present-day ocean. There are of course many additional complications which we have not even considered here. In particular, we have focused on the energetics of the barotropic tides. How this translates into vertical mixing is still not understood even for the modern ocean. Presumably, the spatial pattern of vertical mixing intensity will feed back to influence the

MOC, and this in turn will affect stratification, and ultimately tidally induced mixing. To address the possible role of the tides in this dynamic system will require coupling of models that resolve the long timescales of the MOC with high resolution tidal models. To couple these models we must first understand the physics of tidally induced mixing.

[52] Finally, we should emphasize that the challenges in modeling even the modern day tides are considerable. Accurate bathymetry, careful treatment of tidal loading and ocean self-attraction, and a reasonable parameterization of internal wave drag are required to achieve agreement with altimetrically determined open ocean tidal elevations. Accurate modeling of the LGM tides presents a significantly greater challenge. With sea level dropped to LGM levels a greater fraction of the model dissipation occurs in the deep ocean by scattering into internal tides, and model results become even more sensitive to the assumed stratification. Thus even for the LGM, where we have reasonable knowledge of the actual bathymetry but few good constraints on stratification, there are significant uncertainties in our estimates of tidal dissipation. For the more distant past, where even the shape of the ocean basins is poorly known, direct numerical modeling of the tides and tidal dissipation seems likely to be of limited value.

Appendix A: Parameterization of Internal Tide Drag

[53] Here we derive an approximation to the internal tide radiation drag tensor. The internal tide is forced by the barotropic component of vertical velocity [e.g., *Baines*, 1982] $w_{BT}(z) = \mathbf{u} \cdot \nabla Hz/H$ where $-H \le z \le 0$, and $\mathbf{u}$ is the depth averaged horizontal velocity. Following *Llewellyn Smith and Young* [2001], in the limit of small amplitude bottom topography (and ignoring variations of stratification and f with position) the baroclinic bottom pressure $p_{BC}(-H)$ can be given as the convolution of a radially symmetric Green's function $\mathcal{G}_\omega(s)$ and the barotropic vertical velocity at the bottom $p_{BC}(-H) = \mathcal{G}_\omega * w_{BT}(-H)$. Note that in our notation the Green's function gives the internal wave bottom pressure as a function of distance from a "unit magnitude" point source forcing velocity profile (at frequency ω) of the form $w_{BT}(z) = -z/H$. The Green's function can be written in terms of easily calculated vertical mode eigenvalues and eigenvectors for an ocean of uniform depth and horizontally uniform stratification. A slightly simplified version, based on a WKB approximation to the vertical modes can be given explicitly as

$$\mathcal{G}_\omega(\mathbf{x}) = \frac{(\omega^2 - f^2)N_B}{g} \sum_n H_2^0\left(n\pi\left(\omega^2 - f^2\right)^{-1/2}|\mathbf{x}|/H\bar{N}\right), \quad \text{(A1)}$$

where $\bar{N}$ and N_B are the depth average and ocean bottom buoyancy frequencies respectively, and H_2^0 is the zero order Hankel function of the second kind [*Llewellyn Smith and Young*, 2001]. The barotropic/baroclinic energy conversion at a fixed location is then given by

$$E_f = \langle w_{BT}(-H)p_{BC}(-H)\rangle, \quad \text{(A2)}$$

where the brackets denote tidal cycle averages. Further details, and exact expressions (without the WKB approximation) are given in *Llewellyn Smith and Young* [2001].

[54] This theory allows an explicit formulation for the IT drag which is rigorously justifiable for the case of small amplitude bottom topography and laterally homogeneous stratification. Writing the expression for energy conversion more explicitly

$$E_f = \langle \mathbf{u} \cdot \nabla H[\mathcal{G}_\omega * (\nabla H \cdot \mathbf{u})]\rangle = \langle \mathbf{u} \cdot \mathcal{R}_\omega * \mathbf{u}\rangle, \quad \text{(A3)}$$

where

$$[\mathcal{R}_\omega * \mathbf{u}](\mathbf{x}) = \nabla H(\mathbf{x}) \int\int d^2\mathbf{x}' \mathcal{G}_\omega(|\mathbf{x} - \mathbf{x}'|)\nabla H(\mathbf{x}') \cdot \mathbf{u}(\mathbf{x}'). \quad \text{(A4)}$$

In terms of the dissipative stress $\mathcal{F}$ in equation (1) the energy dissipated from the barotropic tide due to radiation of internal wave energy should be $\mathbf{u} \cdot \mathcal{F}_{IT}$. Hence for a fixed frequency ω the IT drag component of dissipative stress can be represented as

$$\mathcal{F}_{IT} = \mathcal{R}_\omega * \mathbf{u} = \mathcal{R}_\omega * \mathbf{U}/H. \quad \text{(A5)}$$

This is linear in the transports $\mathbf{U}$, but is nonlocal in space, and because the kernel of the spatial convolution operator depends on frequency, is also nonlocal in time. Direct use of equation (A5) in a time stepping modeling code is thus impractical, and some approximations must be made. First, since we focus primarily on the M_2 tide, we take $\omega = 1.4052 \times 10^{-4}\text{s}^{-1}$ as a constant. Second, we do the convolution in space once, using the frequency domain barotropic tidal velocity fields $\mathbf{u}$ from a numerical model to calculate $E_f(\mathbf{x})$ as a function of position using equation (A3). Then, we replace convolution with $\mathcal{R}_\omega$ by multiplication with the 2×2 spatially varying drag tensor

$$\mathbf{R}(\mathbf{x}) = E_f(\mathbf{x})|\mathbf{u} \cdot \nabla H|^{-2}(\nabla H)^T \nabla H. \quad \text{(A6)}$$

[55] The linear 2×2 drag tensor $\mathbf{R}$ results in energy dissipation which agrees with the full convolution results for the M_2 tides provided the tidal velocities in the numerical solution are exactly equal to the a priori assumed $\mathbf{u}$ in equation (A6). For our calculation we computed $\mathbf{u}$ by solving the SWE in a series of small overlapping rectangular areas, each 20° on a side, with grid resolution of 1/30°, and open boundary conditions from the global inverse solution TPXO.5. These local solutions are in fact quite similar to TPXO.5. The resulting approximate drag tensors $\mathbf{R}$ are thus most appropriate for tidal velocities of the modern ocean.

[56] The iterative scheme used for the SAL convolution suggests a possible refinement of this IT parameterization. Given a solution at iteration n, the currents $\mathbf{u}^n$ could be convolved with $\mathcal{R}_\omega$ to compute IT stress for each modeled tidal constituent. These in turn could be added as extra forcing terms for iteration $n + 1$. A modification, comparable to that used for the SAL convolution, would be to include the local linear drag tensor $\mathbf{R}$ in the model equations, and only add the deviation from this as a forcing. This scheme would in principal allow for a frequency dependent, spatially nonlocal parameterization for IT drag for tidal modeling. Since iteration for the SAL correction is already

required, this would probably not require additional runs of the SWE solver. However, we did not test this refinement.

[57] **Acknowledgments.** This work was supported by the National Aeronautics and Space Administration, and by National Science Foundation grant OCE-9819518 to GDE.

References

Accad, Y., and C. L. Pekeris (1978), Solution of the tidal equations for the M2 and S2 tides in the world oceans from a knowledge of the tidal potential alone, *Philos. Trans. R. Soc. London*, *290*, 235–266.

Adkins, J. F., K. McIntyre, and D. P. Schrag (2002), The salinity, temperature, and $\delta^{18}O$ of the glacial deep ocean, *Science*, *298*, 1769–1773.

Baines, P. G. (1982), On internal tide generation models, *Deep Sea Res.*, *29*, 307–338.

Bell, T. H. (1975), Topographically generated internal waves in the open ocean, *J. Geophys. Res.*, *80*, 320–327.

Bills, B. G., and R. D. Ray (1999), Evolution of the lunar orbit: A synthesis of recent results, *Geophys. Res. Lett.*, *26*, 3045–3048.

Bogdanov, K. T., and V. A. Mugarik (1967), A numerical solution of semidiurnal tidal wave distribution (M2 and S2) in the ocean, *Dokl. Akad. Nauk.*, *172*, 6.

Carrére, L., and F. Lyard (2003), Modeling the barotropic response of the global ocean to atmospheric wind and pressure forcing - comparisons with observations, *Geophys. Res. Lett.*, *30*(6), 1275, doi:10.1029/2002GL016473.

Colbo, K. (2002), Mixing processes near boundaries, Ph.D Thesis, 212 pp., Univ. Victoria, Victoria, B.C., Can.

de Vernal, A., C. Hillaire-Marcel, W. R. Peltier, and A. J. Weaver (2002), Structure of the upper water column in the northwest North Atlantic: Modern versus Last Glacial Maximum conditions, *Paleoceanography*, *17*(4), 1050, doi:10.1029/2001PA000665.

Egbert, G. D., and S. Y. Erofeeva (2002), Efficient inverse modeling of barotropic ocean tides, *J. Atmos. Ocean. Technol.*, *9*, 183–204.

Egbert, G. D., and R. D. Ray (2000), Significant tidal dissipation in the deep ocean inferred from satellite altimeter data, *Nature*, *405*, 775–778.

Egbert, G. D., and R. D. Ray (2001), Estimates of M2 Tidal Energy Dissipation from TOPEX POSEIDON Altimeter Data, *J. Geophys. Res.*, *106*, 22,475–22,502.

Egbert, G. D., and R. D. Ray (2003), Semidiurnal and diurnal tidal dissipation from TOPEX/POSEIDON altimetry, *Geophys. Res. Lett.*, *30*(17), 1907, doi:10.1029/2003GL017676.

Egbert, G. D., A. F. Bennett, and M. G. G. Foreman (1994), Topex/Poseidon tides estimated using a global inverse model, *J. Geophys. Res.*, *99*, 24,821–24,852.

Garrett, C., S. Stringer, and L. St. Laurent (2002), Simple models of internal tide generation at abrupt topography, Ocean Science Meeting, Amer. Geophys. Union, Honolulu, HI, 11–15 Feb.

Gordeev, R. G., B. A. Kagan, and E. V. Polyakov (1977), The effects of loading and self-attraction on global ocean tides: The model and the results of a numerical experiment, *J. Phys. Oceanogr.*, *7*, 161–170.

Gustafson, K. E. (2001), Comparison of the energy flux to mixing processes via baroclinic wave drag on barotropic tides, *Deep Sea Res.*, *48*, 2283–2296.

Hansen, K. S. (1982), Secular effects of oceanic tidal dissipation on the Moon's orbit and the Earth's rotation, *Rev. Geophys.*, *20*, 457–480.

Hendershott, M. (1972), The effects of solid earth deformation on global ocean tides, *Geophys. J. R. Astro. Soc.*, *29*, 389–403.

Hendershott, M. C. (1977), Numerical models of ocean tides, in *The Sea*, vol. 6, *Marine Modeling*, edited by E. Goldberg et al., pp. 47–95, John Wiley, New York.

Jayne, S. R., and L. C. St. Laurent (2001), Parameterizing tidal dissipation over rough topography, *Geophys. Res. Lett.*, *28*, 811–814.

Kivman, G. A. (1997), Weak constraint data assimilation for tides in the Arctic Ocean, *Prog. Oceanogr.*, *40*, 179–196.

Le Provost, C. (2001), Ocean tides, in *Satellite Altimetry and Earth Sciences*, vol. 69, 267–303, Academic, San Diego, Calif.

Le Provost, C., and F. Lyard (1997), Energetics of the barotropic ocean tides: An estimate of bottom friction dissipation from a hydrodynamic model, *Prog. Oceanogr.*, *40*, 37–52.

Le Provost, C. L., M. L. Genco, F. Lyard, P. Vincent, and P. Canceil (1994), Spectroscopy of the world ocean tides from a hydrodynamic finite element model, *J. Geophys. Res.*, *99*, 24,777–24,797.

Le Provost, C., F. Lyard, J.-M. Molines, M. L. Genco, and F. Rabilloud (1998), A hydrodynamic model improved by assimilating a satellite altimeter derived data set, *J. Geophys. Res.*, *103*, 5513–5529.

Levitus, S. (1999), Levitus 1 982 annual climatology from DODS datasets Goddard DAAC, NASA, Greenbelt, Md.

Llewellyn Smith, S. G., and W. R. Young (2001), Conversion of the barotropic tide, *J. Phys. Oceanogr.*, *32*, 1554–1566.

Lyard, F., and M. L. Genco (1994), Optimization methods for bathymetry and open boundary conditions in a finite element model of ocean tides, *J. Comput. Phys.*, *114*, 234–256.

Munk, W. H. (1997), Once again: Once again—tidal friction, *Prog. Oceanogr.*, *40*, 7–35.

Munk, W. H., and C. Wunsch (1998), Abyssal recipes: II. Energetics of tidal and wind mixing, *Deep Sea Res.*, *45*, 1977–2010.

National Geophysical Data Center (1992), GEODAS CD-ROM worldwide marine geophysical data, *Data Announce. 92-MGG-02*, U.S. Dep. of Commer., Natl. Oceanic and Atmos. Admin., Boulder, Colo.

Pekeris, C. L., and Y. Accad (1969), Solution of Laplace's equation for the M2 tide in the world oceans, *Philos. Trans. R. Soc., London, Ser. A*, *265*, 413–436.

Peltier, W. R. (1993), Time Dependent Topography Through Glacial Cycle, IGBP PAGES/World Data Center-A for Paleoclimatology Data Contribution Series 93-015, NOAA/NGDC, Paleoclimatol. Prog., Boulder, Colo.

Peltier, W. R. (1994), Ice Age Paleotopography, *Science*, *265*, 195–201.

Platzman, G. W., G. A. Curtis, K. S. Hansen, and R. D. Slater (1981), Normal modes of the world ocean: II. Description of modes in the period range 8 to 80 hours, *J. Phys. Oceanogr.*, *11*, 579–603.

Ray, R. D. (1998), Ocean self-attraction and loading in numerical tidal models, *Mar. Geod.*, *21*, 181–192.

Schmittner, A., K. J. Meissner, M. Eby, and A. J. Weaver (2002), Forcing of the deep ocean circulation in simulations of the Last Glacial Maximum, *Paleoceanography*, *17*(2), doi:10.1029/2000PA000591.

Schwiderski, E. W. (1978), Global ocean tides: I. A detailed hydrodynamical interpolation model, *NSWC/DL TR-3866*, Naval Surf. Weapons Cent., Dahlgren, Va.

Shum, C. K., et al. (1997), Accuracy assessment of recent ocean tide models, *J. Geophys. Res.*, *102*, 25,173–25,194.

Sjöberg, B., and A. Stigebrandt (1992), Computations of the geographical distribution of the energy flux to mixing processes via internal tides and the associated vertical circulation in the ocean, *Deep Sea Res.*, *39*, 269–291.

Smith, W. H. F., and D. T. Sandwell (1997), Global sea floor topography from satellite altimetry and ship depth soundings, *Science*, *277*, 1956–1962.

Thomas, M., and J. Sündermann (1999), Tides and tidal torques of the world ocean since the last glacial maximum, *J. Geophys. Res.*, *104*, 3159–3183.

Wunsch, C. (2003), Determining paleoceanographic circulations, with emphasis on the Last Glacial Maximum, *Quat. Sci. Rev.*, *22*, 371–385.

Wunsch, C., D. B. Haidvogel, M. Iskandarani, and R. Hughes (1997), Dynamics of the long period tides, *Prog. Oceanogr.*, *40*, 81–108.

Zahel, W. (1980), Mathematical modelling of global interaction between ocean tides and Earth tides, *Phys. Earth Planet. Inter.*, *21*, 202–217.

G. D. Egbert, College of Oceanic and Atmospheric Sciences, Ocean. Admin. Bldg. 104, Oregon State University, Corvallis, OR 97331, USA. (egbert@oce.orst.edu)

R. D. Ray, NASA Goddard Space Flight Center, Code 926, Greenbelt, MD 20771, USA. (richard.ray@gsfc.nasa.gov)

B. G. Bills, Institute for Geophysics and Planetary Physics, Scripps Institution of Oceanography, UCSD, La Jolla, CA 92093, USA. (bruce.g.bills@nasa.gov)